JOURNAL OF COMPUTATIONAL PHYSICS **132,** 346–361 (1997)
ARTICLE NO. CP965640

Temporal Evolution of Periodic Disturbances in Two-Layer Couette Flow

Adrian V. Coward,*[,1] Yuriko Y. Renardy,*[,†] Michael Renardy,* and John R. Richards‡

*Department of Mathematics and ICAM, Virginia Polytechnic Institute and State University, Blacksburg, Virginia 24061-0123; and ‡Du Pont Central Research and Development, Experimental Station, P.O. Box 80101, Wilmington, Delaware 19880-0101
E-mail: †renardyy@math.vt.edu

Received May 6, 1996

The time-dependent motion for a two-layer Couette flow consisting of fluids of different viscosities is simulated numerically by using an algorithm based on the Volume of Fluid (VOF) method. Interfacial tension is included via a continuous surface force (CSF) algorithm. The algorithm is fine-tuned to handle the motion which is driven by a shear-induced interfacial instability due to the viscosity stratification. The code is validated against linear theory. Two prototypical situations are presented, one at a moderately high Reynolds number and the other at a lower Reynolds number. The initial condition is seeded with the eigenmode of largest growth rate, with amplitudes that are varied from those that capture the linear regime to larger values for nonlinear regimes. Issues of free surface advection and viscosity interpolation are discussed. The onset of nonlinearity occurs at the interface and is quadratic, followed by wave steepening.

1. INTRODUCTION

Liquid-liquid systems exhibit phenomena which form a subject rich in interdisciplinary science. Applications include the production of bicomponent materials and layered films, and the modeling of bicomponent flows through channels and pipes [1, 2]. The overall properties of systems with two fluids are strongly dependent on interface shapes. In order to control and use these systems, we must develop an understanding of the effects of the bulk properties on interface evolution.

Our motivation for studying two-layer Couette flow is that this is one of the simplest of all the shearing flows of two fluids one might consider. This is a model problem which has received much analysis, and has helped in the development of ideas about more complicated two-fluid flows. The problem has also attracted experimental results [3, 4]. We focus on the instability due to viscosity stratification. The jump in the viscosity from one fluid to the other results in the jump in the tangential velocity gradient across the interface, and can be thought of as a viscous counterpart of the Kelvin–Helmholtz instability.

A difficulty in the theory of flows involving more than one fluid lies in the nonuniqueness of solutions, and the question of which interface shapes would be observed. A first step toward the answer concerns the stability of certain families of interfacial shapes that are observed in experiments. In two-layer Couette flow, the base velocity profile is linear in each fluid with a flat interface. Linear stability analysis of this family of solutions establishes windows in parameter space where the solution may be observed. At the onset of a finite wavenumber instability, the weakly nonlinear analysis of [5] determines whether the time-periodic traveling wave solution would saturate nonlinearly. This analysis determines windows of parameters where, for sufficiently small amplitude perturbations and over long times, the traveling wave solution is expected. These results are described in Section 2. Past the weakly nonlinear regime, a fully numerical simulation is required. We are further interested in predicting wave bending and breakup, past the point of pinch-off of drops, and we require a method which handles easily the breakup and reformation of interfaces. In this sense, the methods that have been used to predict liquid-liquid jet breakup and subsequent formation of satellite drops are of relevance. Examples include the front tracking [6–9] and volume tracking methods [10–12] which include the volume of fluid scheme. The VOF function is defined as zero in one fluid and one in the other, and makes a smooth transition from zero to one through a thin interfacial region commensurate with the mesh spacing. Recently, a new code called "Surfer" [13–15] has been developed to simulate two- and three-dimensional flows with several fluid phases and free interfaces between them. Among the flows they simulate are sheared liquid-gas interfaces subject to the Kelvin–Helmholtz instability. There are differences and similarities between Surfer and our code and it would be

[1] Current address Tessella Support Services plc, 3 Vineyard Chambers, Abingdon 0X143PX, U.K.

0021-9991/97 $25.00

of interest to compare the two in the future. Another scheme that is under development for two-layer flows is that of [16] based on the level-set method.

An algorithm for the VOF method was developed in a two-fluid code called SOLA-VOF [17] which is suited for high Reynolds number gas-liquid flows, but is found to be unstable for the calculation of the surface tension forces in the liquid-liquid jet problem [18]. A one-fluid code, RIPPLE, has been introduced [11] which incorporates the one-fluid VOF algorithm and the continuous surface force formulation to incorporate surface tension. In the CSF method, interfacial surface forces are incorporated as body forces per unit volume in the momentum equations rather than as boundary conditions. Instead of a boundary condition applied at a discontinuous interface, a volume force is used which acts on fluid elements lying within a transition region of finite thickness. These codes have been extensively modified and combined to handle a liquid-liquid jet problem in [18–20], and the resulting VOF/CSF code has been used to predict the experimental data of a jet of an alkane injected into a tank of stationary immiscible water. Though this flow at first glance appears to be essentially the same as the two-layer Couette flow, the mechanisms that drive the unsteady motion are different: jet breakup is driven by surface tension, while interfacial evolution in the two-layer Couette flow is driven by the jump in shear rates across the interface. This necessitates the additional issues described in Section 3, on improvements on how to compute the viscosity when the interface lies within a cell, and the introduction of a Galilean transformation to eliminate numerical instability in the free surface advection algorithm.

Section 4 concerns numerical results with periodicity in the streamwise direction. This is the first validation of linear theory against numerical simulations for two-layer Couette flow. To measure the deviation from the base flow, we use two norms: the maximum of the vertical component of the velocity and its L_2 norm. These are zero in the base flow. The max norm is a pointwise measure of the worst deviation, while the L_2 norm is an averaged quantity, reflecting the behavior of the bulk of the fluid. These diagnostic tools elucidate the region where the nonlinearity first begins.

We focus on specific flow conditions, and results on trends as the conditions are varied are left for future work. The initial conditions are eigenfunctions derived from the linearized stability analysis of the base Couette flow. An important feature is that the location where the first nonlinearity arises is the interfacial region. For weak nonlinearity, quadratic behavior is found to be dominant. The interface and its neighboring region give birth to the nonlinearity while the bulk of the fluid behaves linearly, even for rather small initial amplitudes. The wave steepening is found to occur well before any saturation in amplitude. Results are also shown for regimes where the waveform is highly nonlinear. The wave shapes found in the numerical simulations are qualitatively similar to those seen in experiments [3, 4].

The problem studied here provides a rather sensitive test for the numerical code in two respects: First, viscosity difference at the interface is the crucial factor driving the flow rather than an incidental feature to a flow which is driven by other mechanisms. We have found that the physically correct viscosity interpolation in cells overlapping the interface is important. We were able to incorporate this by a minor modification of the code, under the presumption that the interface is nearly horizontal. In more general geometries where the interface is not aligned with the coordinate axes, the correct viscosity interpolation is much more complicated. Our results show that, at least for the class of problems studied here, such an effort would be worthwhile in future improvements of the code. A second essential feature of our problem is that the interface shape propagates essentially as a traveling wave, with a deformation occuring on a much slower time scale. As a result of this, we found totally useless results unless we introduced a Galilean transformation to a frame moving with the fluid on the interface. This is so even though our code satisfies all of the usual numerical stability conditions. Even with the Galilean transformation, our results show an unphysical formation of steps in the long term. The findings underscore the need for more accurate tracking of the interface. Higher order methods of interface representation [13–15, 27–29, 31] need to be explored.

As a final comment, we note that interfacial instabilities like the one studied here will often lead to three-dimensional structures, see, e.g., [21, 32, 33]. Hence three-dimensional simulations will ultimately be needed.

2. STABILITY THEORY FOR TWO-LAYER COUETTE FLOW

We consider plane Couette flow of two layers of immiscible fluids with different viscosities (see Fig. 1). In dimensionless variables (x, z), the lower fluid is fluid 1 (with viscosity μ_1) and occupies $0 < z < l_1$ in equilibrium. We denote the average depth of the upper fluid, or fluid 2 with viscosity μ_2, by $l_2 = 1 - l_1$. The governing equations are the Navier–Stokes equations and incompressibility in each fluid. At the interface, the kinematic free surface condition holds, velocity and shear stress are continuous, and the jump in the normal stress is balanced by interfacial tension and curvature. There are four parameters: the viscosity ratio $m = \mu_1/\mu_2$, the average depth of the lower liquid l_1, the interfacial tension parameter $T = S^*/(\mu_2 U_i)$ where S^* is the interfacial tension coefficient and U_i is the dimensional interfacial speed of the base flow, and a Reynolds number based on the lower fluid $R_1 = U_i l^* \rho_1/\mu_1$, where l^* is the dimensional plate separation. The velocity distance,

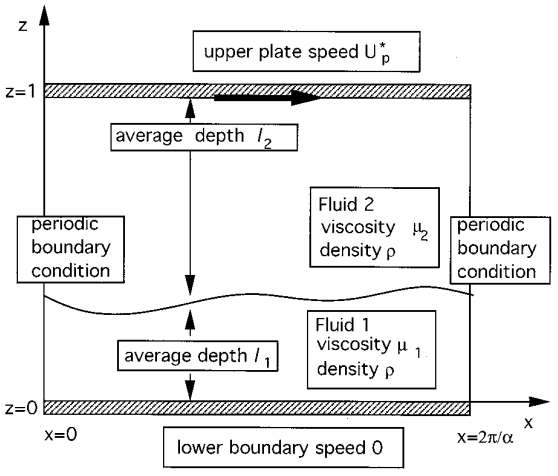

FIG. 1. Flow configuration for two-layer Couette flow, $0 < z < 1$, $0 < x < 2\pi/\alpha$.

time, and pressure are made dimensionless with respect to U_i, l^*, l^*/U_i, and $\rho_1 U_i^2$ as in [5, 21, 22]. With equal densities, gravitational force is balanced by a pressure gradient and can be neglected. One solution to the governing equations is the base velocity field $(U(z), 0)$ where

$$U(z) = \begin{cases} z/l_1, & 0 \le z \le l_1, \\ (m/l_1)(z-1) + U_p, & l_1 \le z \le 1, \end{cases} \quad (1)$$

where the dimensionless upper plate speed is $U_p = 1 + ml_2/l_1$, and the base pressure field is a constant. The stability of this solution is addressed for periodic disturbances.

2.1. *Linear Theory*

Squire's transformation is well known in the problem of stability of shearing flows of one fluid, where it guarantees that the smallest critical Reynolds number will occur when the disturbances are two-dimensional in the plane of the flow. There is a Squire's transformation for the two-layer problem (see Chapter 4 of [1]). Hence, the onset of instability also involves a two-dimensional disturbance, as long as one is dealing with a situation where the flow is stable at low Reynolds numbers and loses its stability as the Reynolds number is increased. This is not always the case in two-layer flows.

Our linearized stability analysis is performed with perturbations $(u(x, z, t), v(x, z, t))$ to the velocity, $p(x, z, t)$ to the pressure and $h(x, t)$ to the interface height $z = l_1$, proportional to $\exp(i\alpha x + \sigma t)$. In the special case when the two fluids are the same, there is a passive interfacial mode that merely allows the interface to be wavy, leaving the velocity field the same: $(u, v) = 0$, $h = h_0 \exp(i\alpha x)$, $\sigma = -i\alpha$. The stability of the flow in this case is determined by the one-fluid bulk modes. When the fluids have different properties, the interfacial mode begins to play an active role in the stability problem. We compute the eigenmodes with the Chebyshev-tau method following [5].

The effects of viscosity stratification, interfacial tension, and speeds determine the stability of two-layer Couette flow. The relevant equations are written in full in [1] where further references are given. We focus on the situation where the longwaves are stabilized by a favorable viscosity stratification and depths [23], and shortwaves are stabilized by interfacial tension, so that the flow loses stability at a single finite wavenumber α_c. Such onsets are described in [5]. Specifically, Table I of [5] shows an onset at $m = 0.5$, $l_1 = 0.372$, $R_1 = 10$, $T = 0.01$, $\alpha_c = 6.3$ and this is the case that we shall pursue for numerical simulations. The fluids are of equal density and the upper fluid is more viscous than the shallower layer below. Figure 2 shows the growth rate versus wavenumber for the critical situation as well as a moderately higher Reynolds numbers which are relevant for Section 4. The critial mode with $\alpha = 6.3$ in the figure is first destabilized (see $R_1 = 40$ curve) by the viscosity difference and inertia, followed by a decrease in the growth rate ($R_1 = 500$). There are other wavenumbers, for example, 4.0, where this behavior is also evident.

2.2. *Weakly Nonlinear Theory*

At criticality, the two-layer Couette flow with a flat interface loses stability to a Hopf bifurcation, and a traveling wave solution may be stable in the weakly nonlinear regime. Let $\Phi = (u_1, v_1, p_1, u_2, v_2, p_2, h)$ represent the difference between the total solution and the basic solution. Subscripts i denote fluid i. For small Φ, the equations and boundary conditions governing the problem are schematically expressed as $L\Phi = N_2(\Phi, \Phi) + N_3(\Phi, \Phi, \Phi)$,

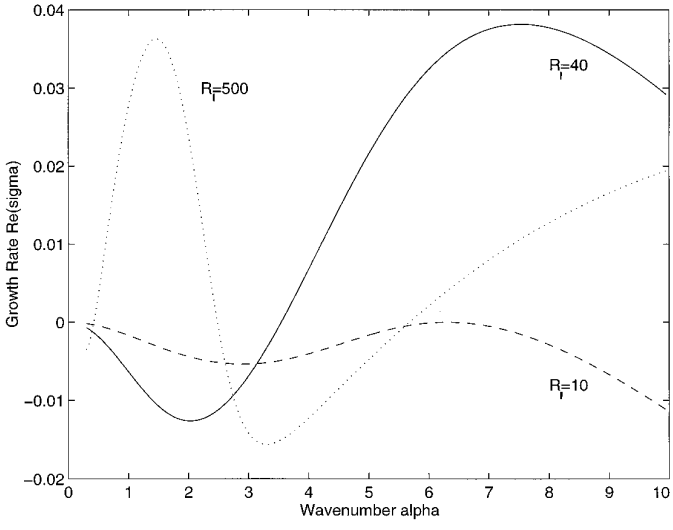

FIG. 2. Growth rate $Re(\sigma)$ versus wavenumber α for $m = 0.5$, $l_1 = 0.372$, equal densities, zero gravity, and $T = 0.01$. $R_1 = 10$, dashed line—critical case; $R_1 = 40$, solid line; $R_1 = 500$, dotted line.

where the quadratic operator N_2 derives from the momentum equations and the interface conditions, and the cubic operator N_3 derives from the interface conditions. The critical mode is denoted $\zeta(\lambda)$, where λ denotes a bifurcation parameter, e.g., $R_1 - R_{1c}$, and the eigenvalue is denoted $-s(\lambda)$ for $\lambda > 0$. The dynamics is dominated by $Z(t)\zeta$ plus its complex conjugate, and the second-order interaction terms, where $Z(t)$ denotes the complex time-dependent amplitude function. The amplitude evolution equation is $dZ/dt + s(\lambda)Z = \kappa|Z|^2Z$, where κ denotes the Landau coefficient. There are a number of approaches to calculating the distortion to the mean flow, and the value of the Landau coefficient depends on this. Our approach is to keep the pressure gradient in the flow direction fixed throughout the nonlinear analysis, while the combined volume flux is not fixed. Our VOF code assumes periodicity in the pressures with no condition on the flow rates, so that the presusre gradient is fixed throughout the nonlinear motion.

When $\mathrm{Re}\kappa < 0$, the traveling wave solution is supercritical, i.e., linearly stable with respect to the perturbation with the same wavenumber as itself. In this regime, there is energy transfer to the mean flow mode and the second harmonics, and the amplitude of the bifurcated traveling wave solution equilibrates, independent of the initial amplitude. When $\mathrm{Re}\kappa > 0$, the solution is subcritical and leads to a finite amplitude transition. The analysis of [5] shows that at $m = 0.5$, $l_1 = 0.372$, $R_1 = 10$, $T = 0.01$, $\alpha_c = 6.3$, the bifurcation is supercritical. Specifically, $\kappa = -156 + 980i$. Based on this, increases in initial amplitudes from small to slightly larger should lead to an equilibration to the same Hopf mode with the same amplitude as $t \to \infty$. At yet larger amplitudes, other types of solutions are expected, and a purely computational approach is required to examine time evolution.

3. NUMERICAL IMPLEMENTATION

We begin with the code as described in [18–20, 24]. In this section, we draw attention to the components that required modification, and leave the description of the other components to a minimum.

The VOF method is an Eulerian scheme in which a function $F(x, z, t)$ measuring the composition of the fluid is convected by the flow. This is a scalar function

$$F(x,z,t) = \begin{cases} 0, & \text{fluid 2,} \\ p, 0 < p < 1, & \text{interface region,} \\ 1, & \text{fluid 1,} \end{cases} \quad (2)$$

where p denotes the relative volume fraction of fluid 1 in each cell intersected by an interface. The nomenclature for fluids 1 (lower) and 2 (upper) follows [5] and is the reverse for [18, 19]. The viscosity for each cell is obtained from a linear interpolation:

$$\mu = \mu_2(1 - F) + \mu_1 F. \quad (3)$$

In the CSF method, the interfacial tension forces are incorporated as body forces per unit volume in the momentum equations, rather than as interface conditions. This volume force acts on fluid elements lying within a transition region of finite thickness, and approximates a discontinuous jump in the normal stress at the interface due to surface tension by a continuous transition over the mesh size Δx. This smearing out of the interface leads to artificial diffusion if the mesh is not sufficiently fine (cf. mesh convergence results in Subsection 4.1).

The size of the physical domain in the x-direction is assumed to be equal to the wavelength $2\pi/\alpha$ of the initial interfacial wave. This imposes the obvious limitation on the simulations that the solutions are required to be periodic with the fixed specified wavelength at each time step. The physical domain is embedded in the computational domain as shown in Fig. 3: there are two columns of fictitious cells on the right of the physical boundary ($I = IMAX$-1, $IMAX$), one row at the top ($J = JMAX$), one on the left boundary ($I = 1$), and the bottom boundary ($J = 1$). The physical domain extends over $I = 2$ to $IMAX$-2 and $J = 2$ to $JMAX$-1. The extra cells surrounding the

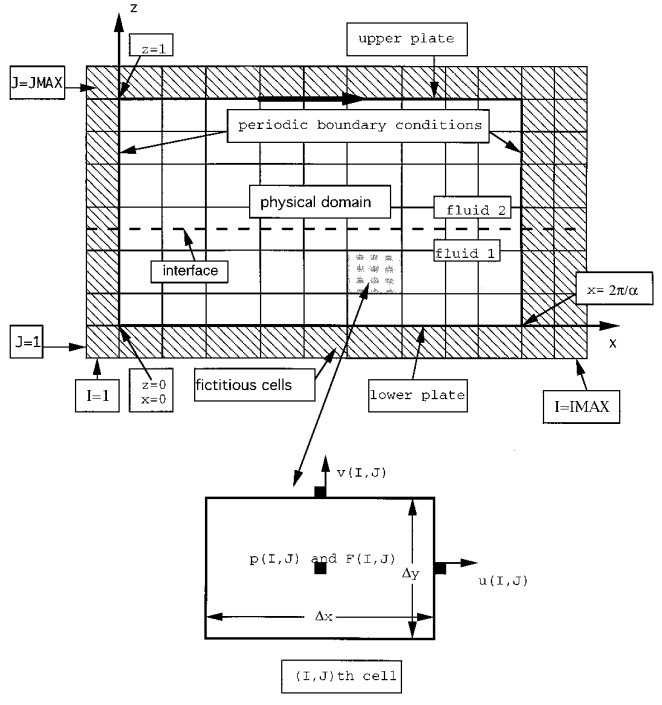

FIG. 3. The upper picture shows the mesh for the computational domain. The fictitious cells are shaded. The physical domain is the unshaded region $0 \le x \le 2\pi/\alpha$, $0 \le z \le 1$. The lower sketch shows a cell.

physical domain are necessary for computing derivatives. A cell is also shown in Fig. 3. The x-component of the velocity is computed at the midpoint of the right hand side of each cell, the z-component at the midpoint of the top side, and the pressure and F function are evaluated at the center. Spatial periodicity on the left and right hand boundaries is imposed on all the variables (the velocity, pressure, and F function) by equating the variables for $I = 1$ to $IMAX$-2, those of $I = 2$ to $IMAX$-1, and $I = 3$ to $IMAX$. The no slip condition is imposed at the bottom boundary $z = 0$ and the horizontal velocity at the top boundary $z = 1$ is $U_p^* = U_i U_p$ with $U_i = 1$, U_p given below Eq. (1). For the horizontal velocity, the boundary values are determined by averaging the nodal values for $J = 1$ and $J = 2$ (bottom boundary) or, respectively, for $J = JMAX - 1$ and $J = JMAX$ (top boundary), see Fig. 3. The code is based on dimensional equations. The continuity equation is recast as a Poisson-like equation for the discretized pressure update, and discretized divergence-free velocity fields. The momentum equations are

$$\rho\left[\frac{\partial \mathbf{u}}{\partial t} + (\mathbf{u}\cdot\nabla)\mathbf{u}\right] = -\nabla p + \nabla\cdot\tau + S^*\kappa\nabla F, \tag{4}$$

$$\tau_{11} = 2\mu\frac{\partial u}{\partial x}, \quad \tau_{12} = \tau_{21} = \mu\left(\frac{\partial u}{\partial z} + \frac{\partial v}{\partial x}\right), \quad \tau_{22} = 2\mu\frac{\partial v}{\partial z}, \tag{5}$$

where S^* is the surface tension coefficient, κ is the curvature of the interface $\kappa = -(\nabla_S\cdot\mathbf{n})$, $\mathbf{n}$ is the unit normal directed into fluid 1, and ∇_S denotes the gradient within the surface. For the computation, the definition of $\mathbf{n}$ is extended throughout the entire volume as $\mathbf{n} = \nabla F/|\nabla F|$. After doing so, one finds that $\kappa = -\nabla\cdot\mathbf{n}$ (see [24]), where now $\mathbf{n}$ and ∇ are defined as quantities in the bulk. The function F satisfies the kinematic condition

$$\frac{\partial F}{\partial t} + u\frac{\partial F}{\partial x} + v\frac{\partial F}{\partial z} = 0. \tag{6}$$

Briefly, there are three stages at each time step. The first is an explicit representation in the momentum equations to calculate new velocities using the velocity and pressure of the previous time step. Volume forces are computed. Inertial terms use a linear combination of central and upwind finite differences. A parameter α_{HN} control the amount of upwinding, and is 0 for the unstable second-order central differencing and 1 for the overstable first-order upwinding differencing. The parameter α_{HN} provides a trade-off between numerical stability and computational efficiency, α_{HN} can be made adaptive so that at each time step it is α_0 times the minimum value required for stability. For our calculations we typically find the $\alpha_0 = 1.2$ ensures accuracy and robustness. Secondly, pressures and velocities in each cell are adjusted iteratively to satisfy the divergence-free condition by using a successive overrelaxation method. The SOR parameter, denoted OMG ($1 \le OMG < 2$), controls the amount of overrelaxation and is adjusted to minimize the number of iterations for updating the pressure field. For the numerical simultations reported here, we have found that $OMG = 1.8$ is an optimal value, above which the pressure iteration scheme will not converge. The tolerance parameter ε measures how accurately the divergence-free condition is discretely satisfied. The choice of ε depends on the flow parameters, mesh spacing, and time step (which is adaptive and decreases when the Reynolds number is small or disturbances have relatively large amplitudes, see Subsection 3.1). A general "rule of thumb" is to set ε to be 10^{-2} times a typical value of $|\partial u/\partial x|$ or $|\partial v/\partial z|$ [24]. We have carried out sensitivity studies for the parameter ε with a variety of flow parameters, initial conditions, and mesh structures. We have found that $\varepsilon = 10^{-5}$ is sufficiently small. In fact, with $\varepsilon < 10^{-7}$ the iterations may not converge or calculations may become prohibitively slow. The boundary conditions are also satisfied and the velocity and pressure are now at the new time level.

Thirdly, the kinematic condition (6) is used to advect the F function. The algorithm used for this is the SOLA-VOF algorithm of Hirt and Nichols [26]. The interface shape is approximated by straight horizontal lines in each cell (cf. [30]), and donor cell fluxing is used if the motion is primarily tangential to the free surface, while acceptor cell fluxing is used if the motion is primarily normal. We refer to [26] for a detailed description. The choice of donor vs. acceptor cell fluxing is designed to keep the interface sharp while avoiding an artificial steepening [26]. A drawback of the method is its low order accuracy. Indeed, we shall see below that a more accurate tracking of the interface would be desirable. Methods which use a higher order method for tracking the interface have been developed [13–15, 27–29, 31] and it would be of interest for future work to study the impact of higher order accuracy in the problem studied here. Some smoothing of the F function is needed to calculate the curvature and this is done in the CSF algorithm. A minimal amount of smoothing is provided by a single pass ($NSMOOTH = 1$) through the spatial filter. Since these flows are driven by viscosity stratification and not capillary forces (as in the jet breakup problem for instance) further smoothing is not required.

3.1. *Stability Conditions*

The time derivatives in the momentum equations are handled by an explicit difference scheme, which necessitates that the time steps Δt be less than roughly the inverse of the magnitude of the largest eigenvalues of the linearized flow problem. The eigenvalue σ for the interfacial mode, as the wavenumber $\alpha \to \infty$, is $O(\alpha)$ ($O(\alpha^{3/2})$ in the inviscid case), while for the bulk modes it is $O(\alpha^2)$ due to viscous damping. In the discretized problem, the analogy is that

the shortest wavelength $2\pi/\alpha$ is the mesh size $O(\Delta x)$. With equal spacing in both spatial directions, the discrete stability condition which is most restrictive is the one resulting from the viscous terms which requires that Δt should be less than a constant multiple of $(\Delta x)^2$. Specifically, the conditions for stability mentioned in [24] are: (i) material cannot move more than one cell in one time step (Courant condition), (ii) momentum must not diffuse more than one cell in one time step, (iii) capillary waves with surface tension cannot travel more than one cell in one time step, (iv) once a time step Δt is chosen, there is a stability condition on α_{HN} which the code adapts. These conditions are, respectively,

$$\begin{aligned} \Delta t &< \begin{cases} \text{min in each cell of } [\Delta x/u, \Delta z/v], \\ 0.5\,(\rho/\mu)\,\Delta x^2\,\Delta z^2/(\Delta x^2 + \Delta z^2), \end{cases} \\ (\Delta t)^2 &< \frac{1}{4S^*}\min(\rho_1, \rho_2)\min(\Delta x^3, \Delta z^3), \\ \alpha_{HN} &= \min[\alpha_0 \max(|u\,\Delta t/\Delta x|, |v\,\Delta t/\Delta z|), 1]. \end{aligned} \tag{7}$$

One difference between the liquid-liquid jet breakup and the two-layer Couette flow considered here is that the latter involves much lower Reynolds numbers, and this necessitates taking smaller time steps due to these stability conditions.

We found that changing to a moving coordinate system was necessary to obtain reasonable results. This is illustrated by Figure 4. The quantities plotted are the maximum norm and L_2-norm of the vertical velocity. The initial condition is the (unstable) interfacial eigenmode with a small amplitude factor superposed on the linear base flow, so that linear growth in time is expected. The solid line shows calculations in the fixed laboratory frame, while the dashed line was done in a frame moving with the unperturbed fluid speed at the interface. Clearly the fixed frame results show spurious oscillations which grow with time. This is accompanied by severe distortion of the interface. The simple remedy of changing to a moving frame removes this problem. The phenomenon illustrated here does not appear to be a numerical instability in the usual sense, since the Courant condition is satisfied even in the fixed frame. However, the accuracy of the advection algorithm for the F function seriously deteriorates if the interface deforms very slowly in time, but at the same time it is convected with the flow on a much more rapid time scale. In order to compute the slow evolution of the interface in a stable and accurate fashion, it is advantageous to eliminate the rapid motion by convection with the flow. All the calculations reported below were done in a frame which moves with the unperturbed interface speed.

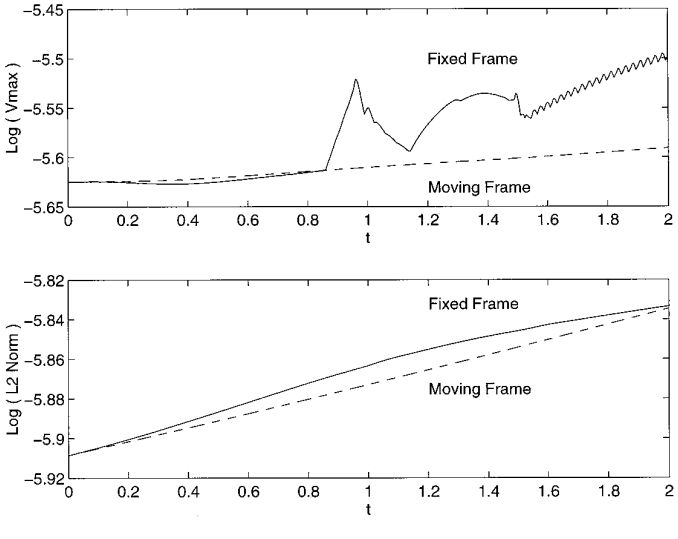

FIG. 4. Comparison of results using a fixed frame (solid lines) and a frame of reference moving at the speed of the unperturbed interface (dashed lines). Upper graph shows $\log(v_{max})$ against time. Lower graph is $\log(L_2$ norm) against time. Flow parameters and initial amplitude are the same as Fig. 8.

3.2. *Initial Condition*

In order to compare with theory, we require the initial velocity field to be continuous and discretely divergence free. Otherwise, the numerical results would be contaminated by extraneous modes or mechanisms. At $t = 0$, the velocity and pressure we input are the base flow (1) plus an eigensolution. The eigenfunction for the velocity, pressure, and perturbation to the interface position, (u_e, v_e, p_e, h), is equal to $\mathrm{Re}[(\tilde{u}_e(z), \tilde{v}_e(z), \tilde{p}_e(z), \tilde{h})\exp(i\alpha x + \sigma t)]$. The Chebyshev-tau scheme is used to discretize the eigenfunction in z, so that $\tilde{u}_e$, $\tilde{v}_e$, $\tilde{p}_e$ have the form of, e.g.,

$$\tilde{v}_e = \begin{cases} \Sigma_0^N a_{n1} T_n(z_1), & z_1 = (2/l_1)z - 1, \\ \Sigma_0^N a_{n2} T_n(z_2), & z_2 = (2/l_2)(z-1) + 1, \end{cases} \tag{8}$$

where z_i denotes the z-variables in each fluid which have been rescaled to $[-1, 1]$. the value N is convergence tested. The discretized eigenvector consists of the coefficients of the Chebyshev polynomials for each unknown, plus $\tilde{h}$; the vector is normalized within the NAG routine F2GJF.

The eigenfunction computed from the linear stability problem is defined over $0 < z < l_1$ for fluid 1 and over $l_1 < z < 1$ for fluid 2, as in Eq. (8). However, the domain occupied by fluid 1 is $0 < z < l_1 + h$ and that of fluid 2 is $l_1 + h < z < 1$. To use the eigenfunction as an initial condition, we need to map it to the perturbed domain. A simple stretching of coordinates has the disadvantage that it destroys the divergence condition. For this reason, we

input our initial condition for the velocity in fluid 1 as

$$(u,v)(x,z) = \left(\frac{l_1}{l_1 + h(x)}\, u_e(x,\zeta_1), v_e(x,\zeta_1) + \frac{\zeta_1 h'(x)}{(l_1 + h(x))}\, u_e(x,\zeta_1)\right). \tag{9a}$$

Here (u_e, v_e) is the velocity field of the eigenfunction, defined on the unperturbed region $0 < z < l_1$ and $\zeta_1 = zl_1/[l_1 + h(x)]$. The analogous expression for fluid 2 is

$$(u,v)(x,z) = \left(\frac{l_2}{l_2 - h(x)}\, u_e(x,\zeta_2), v_e(x,\zeta_2) - \frac{(\zeta_2 - 1)h'(x)}{(l_2 - h(x))}\, u_e(x,\zeta_2)\right), \tag{9b}$$

where $\zeta_2 = 1 + (z - 1)l_2/[l_2 - h(x)]$. The advantage of these expressions is that the divergence condition, as well as the continuity of the normal velocity at the interface, are preserved.

Although the initial velocity field thus generated is divergence free at the continuum level, it is not discretely divergence free. At the first time-step, the velocity becomes discretely divergence free, but the pressure field that accompanies it is spurious for the following reason. One side of the discretized Navier–Stokes equations contains the time derivative of the velocity, which is approximated by the difference between the new velocity field and the initial one, divided by the first time step Δt_0, which is small. In principle, the initial velocity field and the velocity field at the first time step should be close to identical, but they are not, because the initial velocity field is continuously divergence free while the new one is discretely divergence free, and this is the main difference. Thus, the approximation to the time derivative of the velocity at this time step is related only to the fact that the initial velocity field was not divergence free, and has little to do with the actual derivative. The new pressure field is computed by balancing its gradient to the other side of the Navier–Stokes equations which is dominated by this time derivative, and so the pressure computed at the first time step is a spurious response. The way we compensate for this is to run the code to the first time step, retrieve the discretely divergence free velocity field, and we use that with the initial pressure field to start the subsequent computation.

3.3. *Viscosity Interpolation*

The evaluation of the viscous stresses in the finite difference code over cells that are intercepted by the physical interface requires that the viscosity be interpolated, and

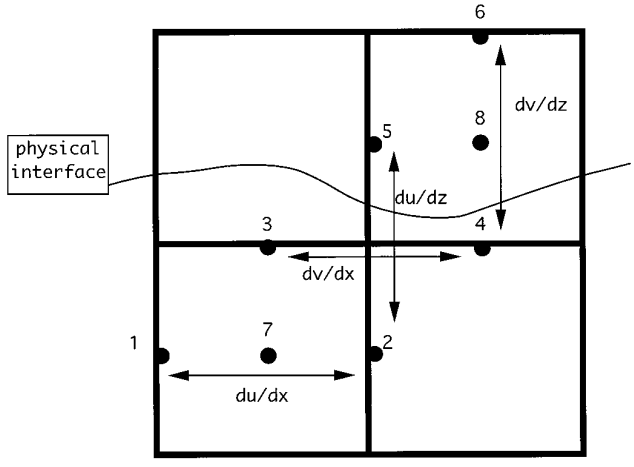

FIG. 5. Definition sketch of grid points used to evaluate finite difference approximation of viscous stresses. The physical interface cuts through the cells as shown. The lower fluid has viscosity μ_1, the upper fluid has viscosity μ_2. v is computed at the midpoint of the upper boundary, and u is computed at the midpoint of the right hand boundary of each cell. $\partial u/\partial x = (u(2) - u(1))/\Delta x$, $\partial v/\partial z = (v(6) - v(4))/\Delta z$, $\partial v/\partial x = (v(4) - v(3))/\Delta x$, $\partial u/\partial z = (u(5) - u(2))/\Delta z$, leading to the computation of τ_{11} at node 7, and τ_{22} at node 8.

there are various ways of doing this. In the finite differencing scheme, the horizontal velocity u is defined at the midpoints of vertical cell edges (e.g., points 1, 2, and 5 in Fig. 5), while the vertical velocity v is defined at the midpoints of horizontal edges (points 3, 4, and 6). From this, one calculates the diagonal components of the stress at cell midpoints, while the shear stress is evaluated at corner points. In the original VOF code, the viscosity for the diagonal stress components is simply taken to be the mean value for the cell (see Eq. (3)), evaluated by using the value of F for the cell, and the viscosity for corner points is found by averaging over the neighboring cells.

This naive interpolation, however, has its drawbacks. Basically, it replaces the average of a product (viscosity times velocity gradient) by the product of the averages, which is badly incorrect for quantities which have a jump across the interface. Better interpolations must take into account which quantities are continuous at the interface and which are not. The issue is discussed in [25] in the context of one-dimensional heat conduction. There, the heat flux is continuous across an interface, while the temperature gradient is not. Along a line segment intersecting the interface, the average of the temperature gradient is therefore approximately equal to the (approximately constant) value of the heat flux times the average of the inverse of the thermal conductivity. Hence taking the harmonic mean of the thermal conductivity is better than straight averaging, which would (incorrectly) set the heat flux equal to the average temperature gradient times the average thermal conductivity.

The fluid dynamic analog is somewhat more complicated, because velocity is a vector and stress is a tensor, and in some components the stress is continuous at the interface, while in others the velocity gradient is continuous. We develop a refined method of viscosity interpolation for the case where the interface is close to being horizontal. If the interface is horizontal, then, because of continuity of velocity, we have continuity of $\partial u/\partial x$, $\partial v/\partial x$, and, because of incompressibility, $\partial v/\partial z$. On the other hand, $\partial u/\partial z$ is not continuous at the interface, but $\tau_{12} = \mu(\partial u/\partial z + \partial v/\partial x)$ is. The basic idea of the following is the same which was used in [25] in the context of heat conduction: The scheme should not replace the average of a product by a product of averages, if both quantities jump across the interface. On the other hand, it is reasonable to multiply the average of a quantity which is discontinuous by the (approximately constant) average of a quantity which is continuous.

The first diagonal component of the stress is (see Eq. (5)) $\tau_{11} = 2\mu(\partial u/\partial x)$, and in the finite difference scheme, $\partial u/\partial x$ is replaced by a difference quotient, e.g., $(u(2) - u(1))/\Delta x$ for the bottom left cell in Fig. 5. This difference quotient is the average value of $\partial u/\partial x$ over the horizontal line segment connecting points 1 and 2. Hence, away from the interface where μ is constant, the scheme replaces τ_{11} by its average over a horizontal line segment. Our viscosity interpolation aims to do the same near the interface. If the interface is nearly horizontal, then u and hence $\partial u/\partial x$ is continuous across the interface, and hence the average of τ_{11} can be approximated by $\partial u/\partial x$ times the average of μ. Motivated by this we chose μ to be the average of the viscosity over the line segment on which the difference approximation for $\partial u/\partial x$ is calculated. For this, we need to know where the interface intersects this line segment, and for that purpose, we used a linear interpolation of the interface position, which is reconstructed from the values of F. The second diagonal component, $\tau_{22} = 2\mu(\partial v/\partial z)$, is treated in an analogous fashion, i.e., μ is chosen to be the average value of μ over a vertical line segment (e.g., the line segment connecting points 4 and 6 for the top right cell in Fig. 5).

The shear stress, $\tau_{12} = \mu(\partial u/\partial z + \partial v/\partial x)$, requires a different treatment. We note that, for a horizontal interface, $\partial u/\partial z$ is not continuous across the interface, but τ_{12} is continuous. We want to select the viscosity value such that this continuity is respected. We can reason that the average of $\partial u/\partial z + \partial v/\partial x$ over any line segment crossing the interface is the (approximately constant) value of τ_{12} times the average of $1/\mu$. For the shear stresses, we therefore used a viscosity value which is obtained by averaging $1/\mu$ over the line segment used to calculate the difference quotient for $\partial u/\partial z$ (e.g., the line connecting points 2 and 5). We note that if the interface is horizontal, then only $\partial u/\partial z$ is discontinuous, while $\partial v/\partial x$ is continuous at the interface. Hence, even though the code replaces $\partial v/\partial x$ by its average on the line from 3 to 4, this average would not differ substantially from the average on the line from 2 to 5.

For future improvements of two-layer codes, it would be advantageous to develop an analogue of this viscosity interpolation scheme which is applicable to arbitrary interface shapes. As above, one needs to make a distinction between those components where the stress is continuous at the interface and those where the velocity gradient is continuous. However, since these components are in general not aligned with the Cartesian grid, a much more complicated algorithm would need to be developed.

The physically correct viscosity interpolation is important particularly in flows where the viscosity jump at the interfaces provides the driving mechanism. While the ''naive'' method of using simple averages for the viscosity works in principle, it may significantly reduce accuracy at the interface.

The importance of viscosity interpolation is illustrated in Fig. 6. The parameters of the simulation are those for case (i) of Table II, and the initial condition is as described in the previous subsection with an initial perturbation to the interface height of $A(0) = 0.001$. We observe two main differences. Firstly, using the refined scheme, $v_{max}(t)$ evolves smoothly from the initial data given by the eigensolutions (dashed line). As time increases, both v_{max} and the L_2 norm grow at a rate close to that predicted by the linear theory. However, the original interpolation method (solid line) produces an initial transient decay which is shown clearly in the expanded graph in Fig. 6. After this

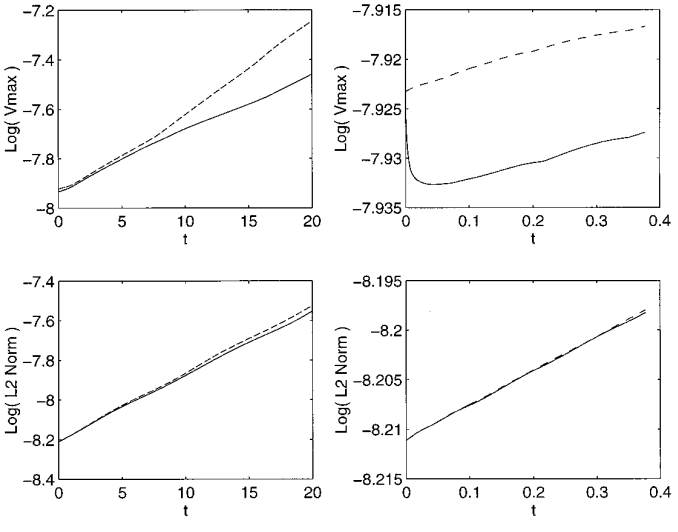

FIG. 6. A comparison of $\log(v_{max}(t))$ using the original (solid line) and improved (dashed line) viscosity interpolations. The improved interpolation has less transient behavior (see the enlarged scales on the right hand side) and shows better correlation with linear theory. $A(0) = 0.001$, $\alpha = \pi/2$, $R_1 = 500$, $m = 0.5$, $l_1 = 0.372$, $T = 0.01$, equal densities, and zero gravity.

short initial decay, both norms grow in time but the magnitude of v_{max} remains uniformly lower than the corresponding norm obtained using the refined interpolation scheme. Secondly, after a relatively long time has elapsed ($t > 8$) the max norms (given by the two schemes) begin to diverge and yield quite different solutions. The L_2 norms are initially indistinguishable but these also separate after sufficient time. It is clear that the improved accuracy of our interpolation scheme has an important effect on the long time evolution of the initial data. The error introduced in the interfacial region by the original viscosity interpolation scheme is first seen in the temporal evolution of v_{max} and eventually propagates throughout the bulk of the fluid, contaminating the L_2 norm. In fact, for many flows, we are unable to accurately reproduce the results of linear theory using the original scheme, whereas using the modified method we can capture linear growth with a high degree of accuracy.

4. NUMERICAL SIMULATIONS

The first step is to check that the algorithm reproduces the known theoretical results. These concern the linear and weakly nonlinear regimes for the situation presented in Section 2 ($m = 0.5$ and $l_1 = 0.372$). The base interfacial speed is $U_i = 1.0$, and plate separation is $l^* = 1$. Since the code uses dimensional variables, we fix $\mu_1 = 1.0$, $\mu_2 = 2.0$, and choose an interfacial tension coefficient $S^* = 0.02$ in Eq. (4) so that the nondimensional group $T = S^*/\mu_2 = 0.01$. With this choice of parameters the velocity and pressure remain the same as their dimensional counterparts. The Reynolds number is then prescribed by fixing the dimensional density ($\rho_1 = \rho_2$) of the fluids. For the Reynolds numbers used in Fig. 2, linear stability theory shows that the only unstable eigenvalue is the "interfacial mode." All "bulk modes" are stable, as shown in Table I, for example; thus, we focus on the evolution of an interfacial mode which is unstable due to viscosity stratification. In Subsection 4.2, we investigate the nonlinear regime above criticality. Specifically we consider the four cases labeled (i) to (iv) in Table II.

The initial conditions, described in Subsection 3.2, are normalized so that the interface height is $z = l_1 + A(0) \cos \alpha x$, where $A(0)$ is the initial amplitude and α is the streamwise wavenumber. The initial velocity field is then $(U(z) + (A(0)/\tilde{h})u, (A(0)/\tilde{h})v)$ where $U(z)$ is the base flow (1), and (u, v) is the divergence free eigenvector (9a), (9b). The evolving flow is then analysed using three main diagnostic outputs: the maximum vertical component of the velocity $v(x, z, t)$ at each time step denoted $v_{max}(t)$; the L_2 norm of the time dependent solution; and the profile of the interface, reconstructed from the volume of fluid function, F.

TABLE I

Eigenvalue σ $\alpha = 6.3$	Eigenvalue σ $\alpha = \pi/2$
$0.0040 - 5.8528i$	$0.0358 - 1.2110i$
$-1.0640 - 9.4618i$	$-0.3039 - 1.9682i$
$-1.2226 - 2.9871i$	$-0.3859 - 1.3654i$
$-1.2571 - 7.1705i$	$-0.6977 - 2.0669i$
$-1.6252 - 4.2410i$	$-0.7407 - 1.0511i$
$-1.6467 - 5.8447i$	$-1.1802 - 2.0123i$
$-1.7713 - 8.3939i$	$-1.2233 - 1.0281i$
$-1.8823 - 9.0432i$	$-1.9937 - 1.9596i$
$-2.3489 - 2.9739i$	$-2.2429 - 1.1267i$
$-2.9052 - 8.5604i$	$-2.9947 - 1.9132i$
$-3.3316 - 3.6714i$	$-3.5287 - 1.1972i$
$-4.1611 - 0.8515i$	$-4.2079 - 1.8718i$
$-4.9762 - 0.3712i$	$-5.0801 - 1.2662i$
$-5.5965 - 0.8468i$	$-5.6408 - 1.8191i$

Note. Eigenvalues σ from the linearized stability analysis of two-layer Couette flow, calculated using $N = 80$ Chebyshev polynomials to represent the vertical component of the velocity v_e. For streamwise wavenumbers $\alpha = 6.3$ and $\pi/2$ the first 14 eigenvalues are tabulated beginning with the least magnitudes of $Re(\sigma)$. The first eigenvalue in each column is the interfacial mode; such that $Re(\sigma) = O(\alpha^2)$ as $\alpha \to 0$, $Re(\sigma) = O(-\alpha)$ as $\alpha \to \infty$. The rest of the modes are bulk modes, such that $Re(\sigma) = O(-1)$ as $\alpha \to 0$, $Re(\sigma) = O(-\alpha^2)$ as $\alpha \to \infty$. Other flow parameters are $R_1 = 500$, $T = 0.01$, $l_1 = 0.372$, $m = 0.5$, equal densities, and zero gravity.

4.1. *Linear Regime*

Our code captures the linear regime provided the initial condition is prescribed carefully on a fine mesh using accurate viscosity interpolation over the cells which are intercepted by the interface (see Subsection 3.3) and for sufficiently small initial amplitudes.

We have chosen a moderately large Reynolds number ($R_1 = 500$) to demonstrate the agreement with linear results. Lower Reynolds number runs require smaller time steps due to the stability conditions (7). Specifically we consider cases (i) and (ii) of Table II, which correspond to disturbances with wavenumbers $\pi/2$ and $\alpha = 6.3$, respec-

TABLE II

	Wavenumber α	Reynolds number R_1	Interfacial mode $Re(\sigma)$
(i)	$\pi/2$	500	0.03577
(ii)	6.3	500	0.00398
(iii)	6.3	40	0.03450
(iv)	6.3	10	0.0

Note. The Reynolds number, wavenumber, and corresponding growth rate of the interfacial mode for each of the four cases discussed in Section 4. Flow parameters are $T = 0.01$, $l_1 = 0.372$, $m = 0.5$, equal densities, and zero gravity.

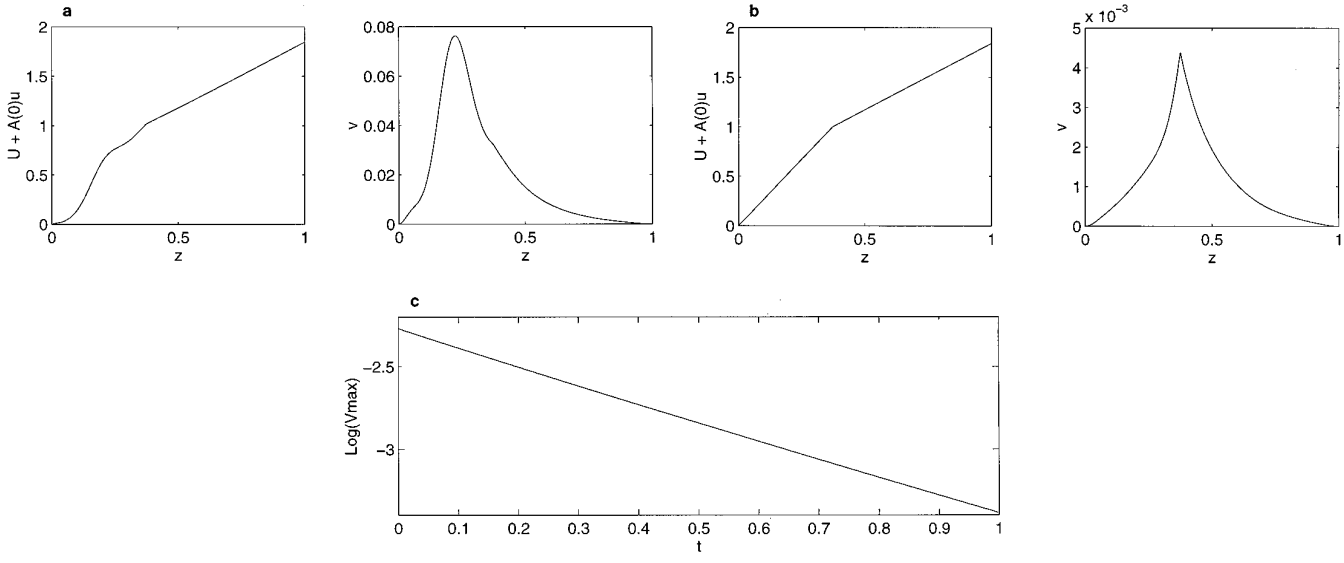

FIG. 7. Initial streamwise (left) and vertical (right) velocity components plotted against the height z from the lower boundary at a fixed point $x = 0.764$ and $t = 0$. (a) The bulk mode with eigenvalue $\sigma = -1.22 - 2.99i$ and (b) the interfacial mode with $\sigma = 0.004 - 5.85i$. (c) Evolution of the log of the max norm from the bulk mode initial condition. The slope of the graph agrees with the decay rate given by linear theory. Flow parameters $A(0) = 0.01$, $\alpha = 6.3$, $R_1 = 500$, $m = 0.5$, $l_1 = 0.372$, $T = 0.01$, equal densities, and zero gravity. Results are converged with an 80×80 mesh.

tively. For case (ii), we see from Table I that the interfacial mode is unstable with a growth rate of $Re(\sigma) = 0.00398$, while all other "bulk-modes" are stable. With $\alpha = \pi/2$ disturbances grow an order of magnitude faster. The complex wavespeed is $\sigma = 0.03577 - 1.2662i$.

The eigenfunctions are normalized so that the perturbation to the interface is $A(0) \cos \alpha x$. The corresponding velocity field for the bulk modes is in general much larger in magnitude than the interfacial mode over the bulk of the flow, whereas the interfacial mode is concentrated in the interfacial area. The bulk modes are therefore easier to resolve spatially. In Figs. 7a–7c we consider a flow with Reynolds number 500, wavenumber 6.3, and initial amplitude $A(0) = 0.01$. In both Figs. 7a and 7b we plot the streamwise and vertical components of the velocity against the normal coordinate z at the point $x = 0.764$ and $t = 0$. The upper and lower plates are at $z = 1$ and 0, respectively, and the base flow $(U(z), 0)$ is scaled so that $U(0.372) = 1$. An interesting difference between the eigenfunctions for the bulk and interfacial modes is that for the latter, the maximum vertical velocity occurs at the mean interface position, while for the bulk mode it lies in the lower layer. Comparing the scales in these figures, we notice that the bulk mode, Fig. 7a, with eigenvalue $\sigma = -1.22 - 2.99i$, has a corresponding eigenvector v which, when multiplied by $A(0)$, is 8% of the magnitude of the base flow, whereas for the interfacial mode, shown in Fig. 7b, it is only 0.4%. The bulk mode is thus easier to resolve numerically, and our scheme gives excellent agreement with the linear decay rate, mesh-converged on a relatively coarse mesh with 80×80 cells (see later comments regarding mesh convergence studies). The log of the max norm depicted in Fig. 7c has a slope of -1.22. With other wavenumbers and Reynolds numbers we have observed equally good agreement with bulk modes. Perturbations to the base state again decay exponentially, according to $\exp[Re(\sigma)t]$.

More spatial accuracy, and refinements on free surface advection and viscosity interpolation, are required in order to capture the growth or decay of the interfacial mode. In addition we require a smaller initial amplitude in order to suppress the onset of nonlinearity. For case (i), Fig. 8 shows the evolution of the interfacial mode with an amplitude $A(0) = 0.01$. The lower graph of Fig. 8 shows the log of the L_2 norm against time for a coarse and fine mesh. The upper two plots show the log of v_{max} against time. The max norm is most sensitive to the spacing of the mesh in the z direction (see center graph). Typically about 160 grid lines are required along the vertical axis to achieve mesh convergence. Less refinement is required in the streamwise direction, v_{max} is mesh converged with $\Delta x \leq 0.02$, approximately (upper graph). Note that unless Δx is small, we see regularly spaced cusps along the graph of $v_{max}(t)$. This arises from the motion of the location of the true maximum of the vertical component of the velocity through each cell; the Max(v) is computed at the nodes which are at the midpoint of the top edge of each cell. As the position of maximum v moves through a cell, there is a fluctuation before it reaches the next node. This "ribboned" effect has been correlated with the wavespeeds of the interfacial mode, and decays as the mesh is refined. Over a short

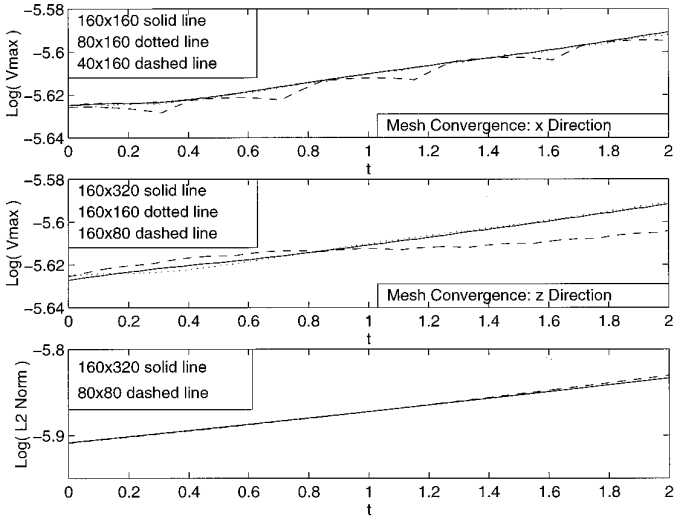

FIG. 8. Max norms and L_2 norms for case (i) of Table II, with initial amplitude $A(0) = 0.01$ calculated using a variety of uniformly spaced meshes: *Upper plot* shows mesh convergence in the streamwise (x) direction for $\log(v_{max})$. 160×160, solid line; 80×160, dotted line; 40×160, dashed line. Note that further mesh refinement in the x direction yields results which are identical to the 160×160 graph. *Center plot* shows mesh convergence in the vertical (z) direction for $\log(v_{max})$. 160×320, solid line; 160×160, dotted line; 160×80, dashed line. *Lower plot* shows mesh convergence for $\log(L_2$ norm). 160×320, solid line; 80×80, dashed line.

period of time at least, the L_2 norm yields almost identical results for all grids with $\Delta x \leq 0.05$, $\Delta z \leq 0.02$. The L_2 norm shows good correlation with the predicted linear growth rate $Re(\sigma) = 0.03577$, since the log of the norm grows linearly at a rate of about 0.036. The maximum vertical velocity is more sensitive to mesh refinement and, perhaps more importantly, the mesh converged max norm does not grow exponentially in time. Although the solid lines in the upper and center graphs of Fig. 8 might appear to have constant slopes, they actually do not. This becomes more evident by looking at the upper graph of Fig. 10, which shows the evolution over a longer time. Nonlinear effects are clearly important here even after a relatively short computation time. In fact, for all flows we have considered, we observe that nonlinearity enters initially in the neighborhood of the interface. The temporal evolution of v_{max} is very sensitive to this onset, while the L_2 norm (which is an average over the entire domain) can remain linear for a considerable time before nonlinearity finally saturates the system.

In other cases, particularly if the growth rate of the interfacial mode becomes very small, further mesh refinement is often necessary to give converged data. For example, with flow parameters given by case (ii) in Table II, we find that although a uniform 320×320 mesh yields results for v_{max} which grow exponentially, we require even more cells along the vertical coordinate in order to obtain complete quantitative agreement with linear theory which describes the competition between the growth of short wavelength disturbances and the stabilizing effect of surface tension. We have not pursued calculations with the cell height $\Delta z < 0.0025$ because of the smallness of time step imposed by numerical stability constraints.

Accurate reproduction of the linear theory for the interfacial mode necessitates a very small initial amplitude $A(0)$. In Fig. 9 we show the linear growth of perturbations with wavenumber $\alpha = 6.3$, Reynolds number $R_1 = 40$, and initial amplitude $A(0) = 0.0001$. The upper two plots show the log of v_{max} and the L_2 norm versus time. After a short initial transient (which is present even when the initial time step is reduced) both norms correlate exactly with the linear analysis which predicts exponential growth with $Re(\sigma) = 0.0345$. Although we illustrate the growth only as far as time $t = 5$, linearity persists until quadratic terms in $A(t)$ become significant. The interface retains its initial cosine shape, moves in the streamwise direction, and grows exponentially in time, as depicted by the lower graph in Fig. 9 which shows the interface height at equal time intervals. Unlike case (ii) discussed above, these results are mesh converged using 160×160 cells. This highlights the need for mesh refinement studies for each situation, both to check the validity of the results, and also to optimize computation times. Note that if we take $O(N)$ cells in each direction, then the computation time is $O(N^4)$, since both the number of degrees of freedom and the required number of time steps (according to the stability condition (7)) increase proportional to N^2.

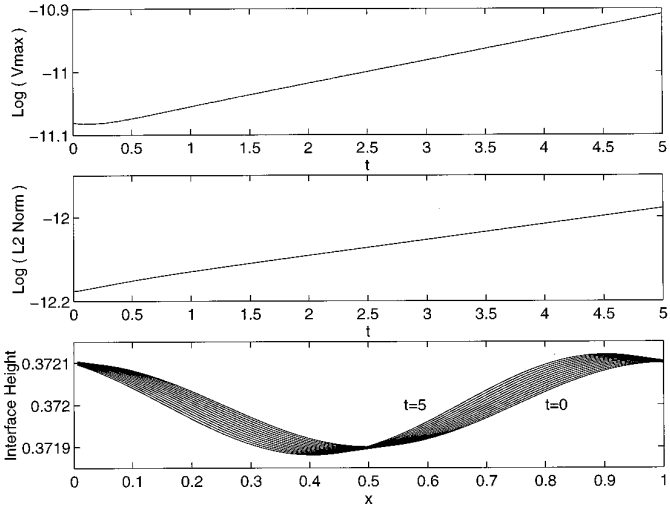

FIG. 9. Log plot of the maximum vertical velocity (upper) and the log of the L_2 norm against time (center) and a plot of the interface position at successive time intervals (lower) for the flow: $A(0) = 0.0001$, $\alpha = 6.3$, $R_1 = 40$, $m = 0.5$, $l_1 = 0.372$, $T = 0.01$, equal densities, and zero gravity. Linear stability analysis indicates that the growth rate for the interfacial mode is 0.0345.

4.2. *Weakly Nonlinear Regime*

The solution at time t is a smooth function of the initial conditions and can be expanded as a power series in the initial amplitude, provided $A(0)$ is sufficiently small. This expansion is not uniform, and, depending upon the other parameters present, breaks down as t becomes large. We use this idea to analyse the onset of nonlinearity. We implement a Richardson extrapolation by expanding v_{max} as a function of the initial amplitude $A(0)$, so that

$$v_{max}(t) = f(t)A(0) + g(t)A^2(0) + O(A^3(0)). \quad (10)$$

For a chosen initial amplitude $A_1 = A(0)$ we calculate the corresponding norm $V_1(t; A_1) = v_{max}(t)$ which evolves nonlinearly in time. Then, with an initial amplitude $A_2 = nA_1$ (for some value n) we calculate $V_2(t; A_2) = v_{max}(t)$. Neglecting cubic terms in Eq. (10), we obtain expressions for the linear and quadratic dependence of v_{max} on t:

$$f(t; n) = \frac{n^2V_1 - V_2}{n(n-1)A_1}, \qquad g(t; n) = \frac{V_2 - nV_1}{n(n-1)A_1^2}. \quad (11)$$

Choosing $A_1 = 0.01$ we see from Fig. 10 that $\log(v_{max})$ grows fairly linearly initially, but as time increases nonlinearity sets in. The corresponding max norm for double the initial amplitude ($n = 2$), $A_2 = 0.02$ shows evidence of nonlinearity much earlier. However, the log plot of the extrapolation function $f(t; n = 2)$ is quite linear for time $0 < t \leq 10$, and has a slope of about 0.036, in agreement with the predicted exponential growth of the form $\exp[Re(\sigma)t]$ for infinitesimally small amplitude perturbations to the base flow. The quantity g calculated in this manner contains, in addition to information on the quadratic terms, other information such as the error by which our initial conditions deviate from being an eigenmode, remapped to $O(h)$ accuracy.

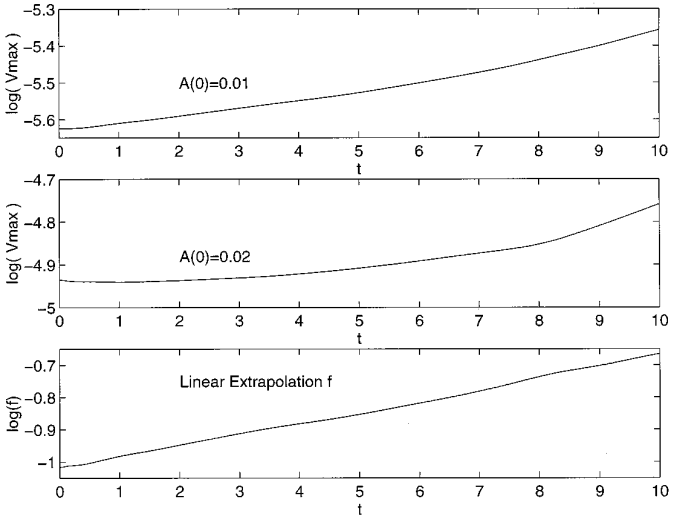

FIG. 10. Log plot of the maximum vertical velocity for amplitudes $A(0) = 0.01$ (upper graph) and $A(0) = 0.02$ (center) against time and the corresponding linear extrapolation f given by Eq. (10) (lower plot), with flow parameters $\alpha = \pi/2$, $R_1 = 500$, $m = 0.5$, $l_1 = 0.372$, $T = 0.01$, equal densities, and zero gravity.

4.3. *Wave Steepening Regime*

We now consider the nonlinear regime; specifically, we analyse the temporal development from initial conditions (i) and (iii) in Table II. For both cases we have conducted numerical experiments with initial amplitudes ranging from $A(0) = 0.0001$ to 0.05. Our mesh convergence studies have shown that a uniformly spaced 160×160 grid yields identical results to those computed using finer meshes. Optimal values for the parameters OMG, α_0, $NSMOOTH$, and ε are found to be 1.8, 1.2, 1, and 10^{-5}. The initial conditions, given by the eigensolution of linear theory, are mapped onto the perturbed domain, as described by Eq. (9a) in Subsection 3.2. The "refluxing" of the initial pressure ensures a divergence free velocity field which then evolves on a frame of reference which moves at the constant speed of the unperturbed interface. In Figs. 11a, 11b and 12a, 12b we show the "long time" development of perturbations with streamwise wavenumber $\alpha = \pi/2$ and supercritical Reynolds number 500. For this situation, case (i), we observe the following trends. Small initial amplitude perturbations to the base state grow linearly in time. The interface slowly evolves from the initial $\cos(\pi x/2)$ shape, travels in the streamwise direction, and grows in amplitude. When $A(0) \leq 0.001$ this growth is close to exponential in accordance with linear theory.

With $A(0) > 0.01$, nonlinear effects become important almost immediately. A careful analysis of the two norms shows that this onset occurs near the interface and gradually propagates throughout the bulk of the two fluids. In Figs. 11a and 12a we show the evolution of both norms and the location of $v_{max}(t)$ for initial amplitudes $A(0) = 0.03$ and 0.05, respectively. For both cases, the L_2 norms show linear growth over a significant time while v_{max} evolves nonlinearly. With $A(0) = 0.03$ the upper left graph of Fig. 11a shows how $\log(v_{max})$ initially decays and then grows. The streamwise location of the maximum vertical component of velocity moves along with the interfacial wave. Initially v_{max} occurs at the nearest mesh point to the crest of the wave which, as shown in Fig. 11b, evolves smoothly from its initial height $z = 0.372 + 0.03 \cos(\pi x/2)$ labeled $t = 0$. As time increases, the wave develops a steep narrow trough, and location of the max norm moves towards the wave steepening region (see bottom right plot of Fig 11a). The interfacial profiles shown in Fig. 11b are plotted at equal time intervals. We noted that

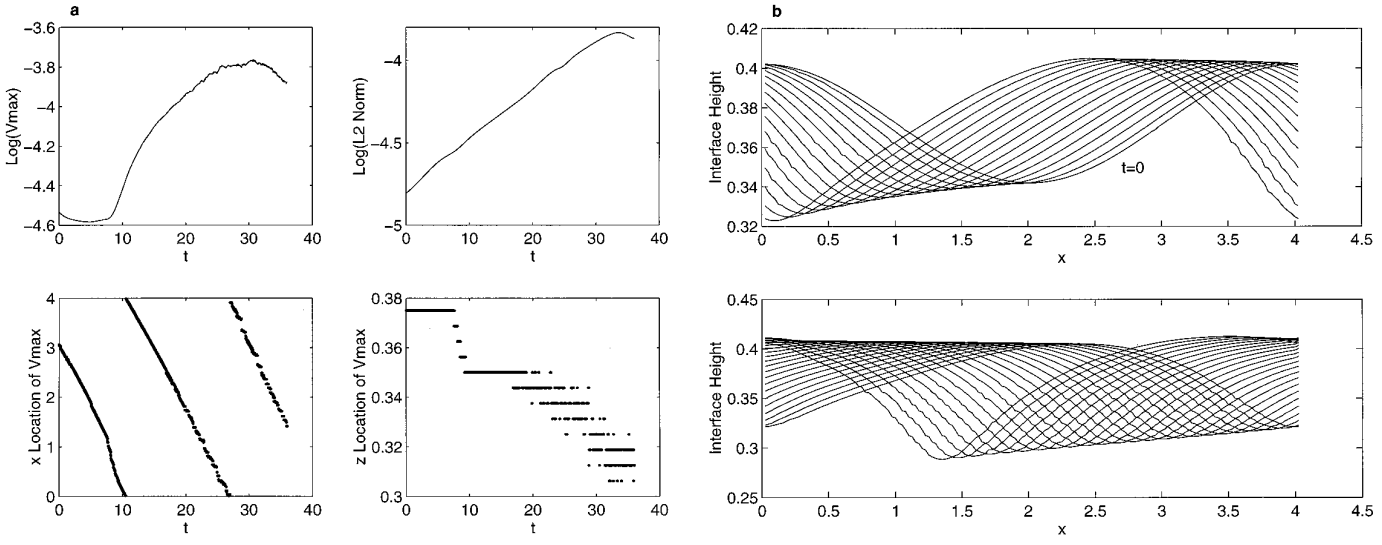

FIG. 11. (a) Log plot of v_{max} and L_2 norms against time (top left and top right, respectively). The x and z location of v_{max} are shown on the bottom left and right, respectively. Initial amplitude $A(0) = 0.03$, wavenumber $\alpha = \pi/2$, Reynolds number $R_1 = 500$. Other flow parameters $m = 0.5$, $l_1 = 0.372$, $T = 0.01$, equal densities, and zero gravity. (b) Gradual onset of nonlinearity leading to wave steepening of the interface. The initial interface height is $z = 0.372 + 0.03\cos(\pi x/2)$. The early development for $0 \le t \le 14$ is illustrated in the upper plot; the lower plot shows $14 < t \le 36$. Profiles are shown at equal time intervals. Flow parameters as in Fig. 11a.

although the interface appears to move in the negative x direction at a speed of approximately -0.25, this is with respect to a frame of reference which moves along in the streamwise direction at the speed of the unperturbed interface. Hence the interface in the original fixed frame actually moves in the positive x-direction with a speed of approximately 0.75. The upper plot of Fig. 11b shows successive interface heights for $0 \le t \le 14$ and the lower graph shows subsequent evolution $14 < t \le 36$.

For a larger initial amplitude, $A(0) = 0.05$, the wave steepens more rapidly and is accompanied by strong decay in v_{max} until $t = 7.7$ (see Figs. 12a, 12b). Beyond this point the max norm shifts away from the crest of the interface to the narrow trough where the rapid change is taking

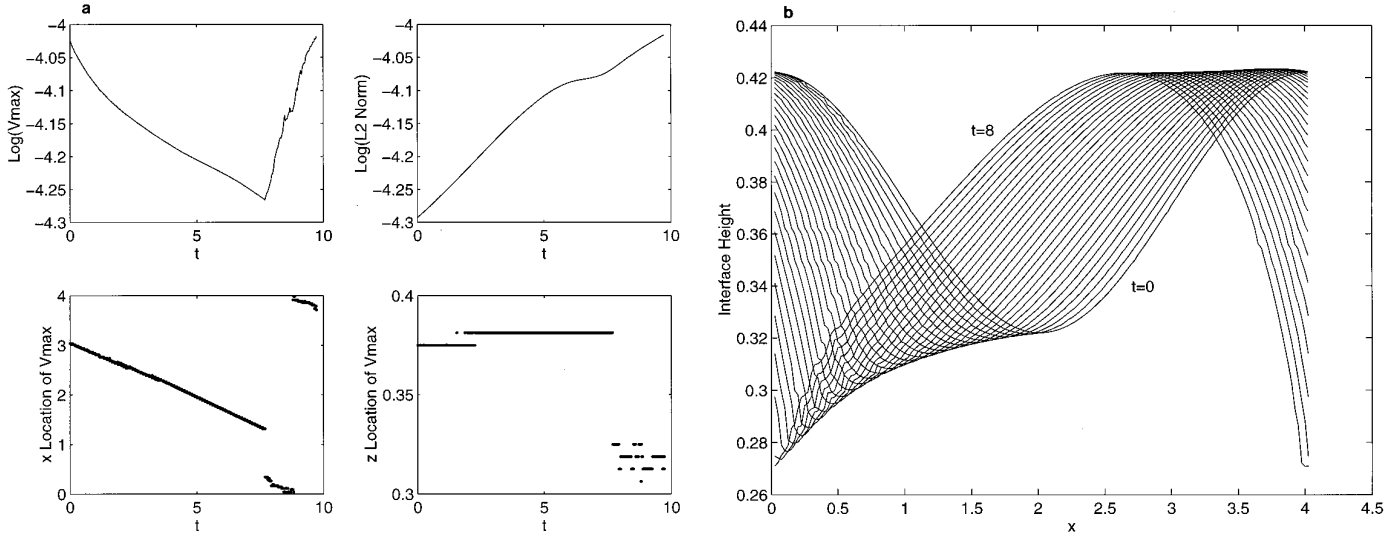

FIG. 12. (a) Log plot of v_{max} and L_2 norms against time (top left and top right, respectively). The x and z location of v_{max} are shown on the bottom left and right, respectively. Initial amplitude $A(0) = 0.05$, wavenumber $\alpha = \pi/2$, Reynolds number $R_1 = 500$. Other flow parameters $m = 0.5$, $l_1 = 0.372$, $T = 0.01$, equal densities, and zero gravity. (b) Nonlinear wave steepening of the interface for $0 \le t \le 8$. The initial interface height is $z = 0.372 + 0.05\cos(\pi x/2)$. Other flow parameters as in Fig. 12a.

place. The interfacial perturbation spans 10% of the domain initially and as it evolves it grows in amplitude. The trough of the wave narrows significantly and continuing the calculations for longer times may therefore require further spatial refinement.

In Fig. 13 we examine a situation closer to criticality, case (iii) with $R_1 = 40$, $\alpha = 6.3$, and $A(0) = 0.01$. Again we see an interfacial wave which develops a deep trough with a long flat crest. The wave moves in the streamwise direction slightly slower than the base speed of the unperturbed interface. The calculations require a small time step due to the numerical stability constraints imposed for low Reynolds number simulations. We note that the wave shape found in the numerical simulations is in good qualitative agreement with the experimental data given in [3, 4]. In particular, the data shown in Figs. 7a, 11, and 12 of [3] show similar wave distortion with steep fronts and sharp troughs, albeit in a saturated regime: Our numerical results on the other hand lie in the transient regime. With lower Reynolds numbers approaching the critical case (iv) of Table II, the time for saturation to take place theoretically becomes longer, and this was also found experimentally in Fig. 14 of [3]. Their data also suggest that saturation would be expected for higher Reynolds number cases. However, we have not been able to follow the interface evolution to the point where the amplitude saturates for the following reason.

In the wave steepening regime, the advection algorithm leads to a "step" structure of the interface, where the shape flattens or steepens discretely along grid lines; this is due to a lack of accuracy in the scheme. The beginnings of this are visible in Figs. 11–13, and the phenomenon worsens as the wave steepens further. This is illustrated in Figs. 14a, 14b, which show case (iii) with initial amplitude $A(0) = 0.05$ at time $t = 2$. Figure 14b uses a finer mesh in the interfacial region; a quadratically spaced mesh is used where Δz_{min} is prescribed at $z = l_1$ and the number of mesh points above and below this are specified. Both types of viscosity interpolation schemes were used and produced similar results. The effect also worsens as the Reynolds number is lowered. Figure 14c shows computations for case (iv) of Table II, which is a critical situation according to linear theory. We see that the interface almost immediately develops into a step structure. The initial amplitude here is $A(0) = 0.005$, so that the interface spans three cells vertically. As evident in the mesh refinement results of Figs. 14a, 14b, severe mesh refinement in a neighborhood of the interface would avoid this problem. However, even with variable meshes this would be computationally impractical, since the time step according to the stability condition is determined by the smallest cell size. Hence a more accurate tracking of the interface location is required for further progress. We emphasize that the formation of steps which we observe here is not the instability phenomenon which was observed by Hirt and Nichols [26] when acceptor cell fluxing was used. Indeed, our code is based on the SOLA-VOF algorithm which was advocated by Hirt and Nichols to avoid such instabilities. The problem we are encountering seems to be one of accuracy rather than stability. Higher order methods of interface tracking [13–15, 27–29, 31] may be useful in overcoming this difficulty.

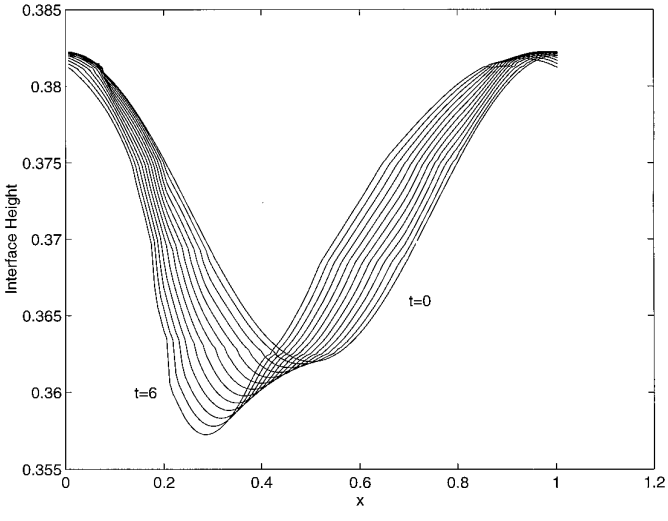

FIG. 13. Plots of the interface position at equal intervals for $0 \le t \le 6$. The onset of nonlinearity leads to rapid wave steepening. Initial amplitude $A(0) = 0.01$, for a flow with wavenumber $\alpha = 6.3$, Reynolds number $R_1 = 40$, $m = 0.5$, $l_1 = 0.372$, $T = 0.01$, equal densities, and zero gravity.

It is particularly instructive to comment on the formation of steps in the interface for case (iv), Fig. 14c, which is an onset condition. Here, the growth rate is virtually zero, so the interface is not moving in the vertical direction. However, the interface is subjected to horizontal shearing. The steps results from the fluid in each cell moving horizontally, the cells at the same vertical level moving at the same speed, resulting in horizontal strips of one cell height moving each with its own horizontal speed. We believe that the step-like structure forms because the fluid velocity with which the interface is advected, which is determined at discrete locations, namely the midpoints of cell edges, is purely horizontal. This effect is alleviated somewhat in our higher Reynolds number samples, because of the combined vertical and horizontal movements so that fluid particles do not stay within the same horizontal strip of the mesh. When fluid parcels move vertically as well as horizontally, the averaging of the velocity takes place in such a manner that the contours of the F function are more likely to remain smooth. We conclude that future improvements of interface tracking should aim at using more accurate interpolations of interfacial speeds, i.e., the interface should be advected with the speed at the actual interface position rather than a speed which is determined at the midpoint of a gridline.

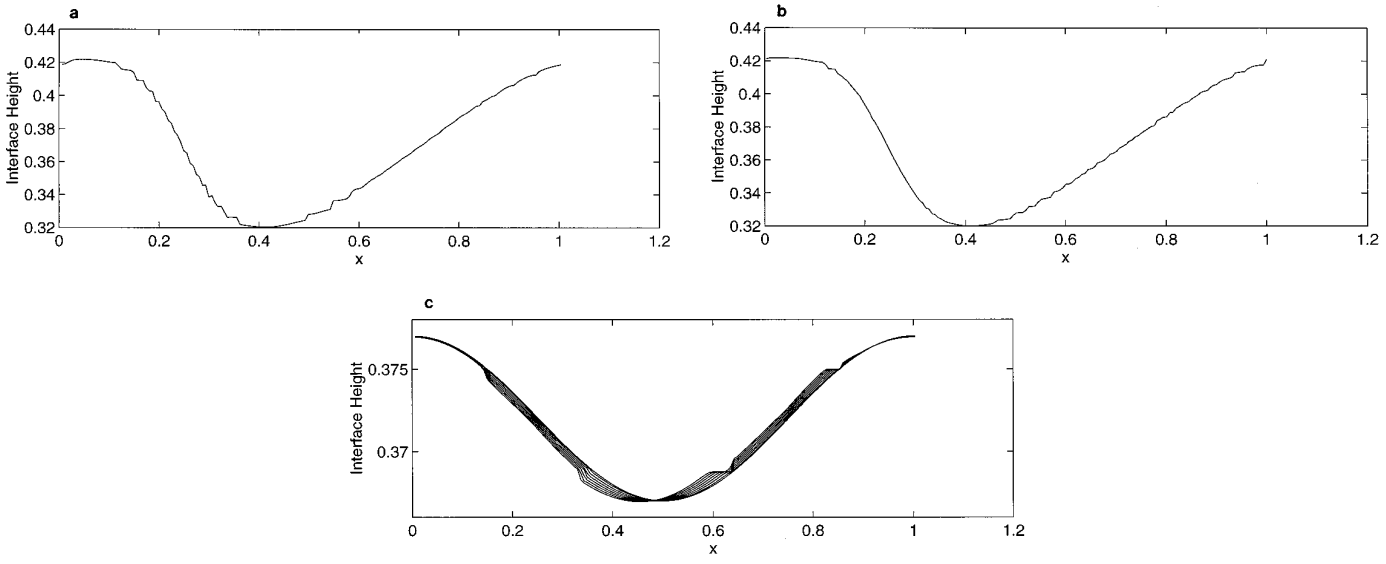

FIG. 14. (a) Uniform 160×160 grid, $\Delta z = 0.00625$. The initial interface height is $z = 0.372 + 0.05 \cos(6.3x)$, $R_1 = 40$, $\alpha = 6.3$. The interface position is shown at $t = 2$. (b) Quadratically graded 160×160 mesh centered at $z = l_1 = 0.372$ with 80 above and below, $\Delta z_{min} = 0.002$. The interface position is shown at $t = 2$. (c) The initial interface height is $z = 0.372 + 0.005 \cos(6.3x)$, $R_1 = 10$, $\alpha = 6.3$. The interface position is shown for $0 \leq t \leq 2$ at equal intervals.

5. CONCLUSION

We have presented a critical assessment of the algorithm based on VOF/CSF, for tracking interface evolution in a spatially periodic viscous-stratified flow. This new application required the following modifications: a Galilean transformation to track the evolution in interface shape which occurs on a slower time scale than the rapid convection of the interface, the construction of a discrete initial condition from the eigenmode of linearized theory, and a refined viscosity interpolation scheme. Our numerical simulations reproduce linear theory. Furthermore, we find that nonlinearity manifests itself initially at the interface, with the maximum pointwise deviation from the base flow being at the wave crest, later moving to the narrow and steep trough.

The algorithm has remaining problems. In the wave steepening regime, the accuracy of the free surface advection algorithm decreases and a modification in the calculation of the F function is necessary for further progress. However, the waveforms we compute in this regime agree qualitatively with the shapes observed in experimental data [3, 4]; thus this approach appears promising.

ACKNOWLEDGMENTS

The authors thank Professor Antony N. Beris for his assistance and advice. This work is funded by the ONR Grant N00014-92-J-1664 and the NSF Grants CTS-9307238 and DMS-9306635. Part of this work was done while the authors were visiting the Isaac Newton Institute, University of Cambridge.

REFERENCES

1. D. D. Joseph and Y. Y. Renardy, *Fundamentals of Two-Fluid Dynamics, Part I, Mathematical Theory and Applications; Part II, Lubricated Transport, Drops and Miscible Liquids* (Springer-Verlag, New York, 1993).
2. D. D. Joseph, R. Bai, K. Chen, and Y. Renardy, *Ann. Rev. Fluid Mech.* **29,** 65 (1997).
3. P. Barthelet, F. Charru, and J. Fabre, *J. Fluid Mech.* **303,** 23 (1995).
4. P. Barthelet and F. Charru, Experimental study of interfacial waves in a two-layer shear flow: Short wave modulations and long wave–short wave interactions, in *Advances in Multi-Fluid Flows,* edited by Y. Renardy, A. V. Coward, D. Papageorgiou, and S. M. Sun (SIAM, Philadelphia, 1996), pp. 13–41.
5. Y. Renardy, *Phys. Fluids A* **1,** 1666 (1989).
6. R. W. Yeung, *Ann. Rev. Fluid Mech.* **14,** 395 (1982).
7. J. M. Hyman, *Physica D* **12,** 396 (1984).
8. S. O. Unverdi and G. Tryggvason, *Physica D* **60,** 70 (1992).
9. S. O. Unverdi and G. Tryggvason, *J. Comput. Phys.* **100,** 25 (1992).
10. M. Sussman, P. Smereka, and S. Osher, *J. Comput. Phys.* **114,** 146 (1994).
11. D. B. Kothe, R. C. Mjolsness, and M. D. Torrey, RIPPLE: A computer program for incompressible flows with free surfaces, Technical Report LA-12007-MS, Los Alamos National Laboratory, 1991 (unpublished).
12. S. Osher and J. A. Sethian, *J. Comput. Phys.* **79,** 12 (1988).
13. B. Lafaurie, C. Nardone, R. Scardovelli, S. Zaleski, and G. Zanetti, *J. Comput. Phys.* **113,** 134 (1994).
14. F. X. Keller, J. Li, A. Vallet, D. Vandromme, and S. Zaleski, Direct numerical simulation of interface breakup and atomisation, in *Proc. Sixth Int. Conf. on Liquid Atomization and Spray Systems,* edited by A. J. Yule and C. Dumouchel (1994), pp. 56–62.
15. J. Li, Calcul d'interface affine par morceaux, *C. R. Acad. Sci. Paris* **320,** 391 (1995).

16. R. R. Yiu and K. P. Chen, Numerical experiments on disturbed two-layer flows in a channel, in *Advances in Multi-Fluid Flows,* edited by Y. Renardy, A. V. Coward, D. Papageorgiou, and S. M. Sun (SIAM, Philadelphia, 1996), pp. 368–382.
17. B. D. Nichols, C. W. Hirt, and R. S. Hotchkiss, SOLA-VOF: A solution algorithm for transient fluid flow with multiple free boundaries, Technical Report LA-8355, Los Alamos Scientific Laboratory, 1980 (unpublished).
18. J. R. Richards, A. N. Beris, and A. M. Lenhoff, *Phys. Fluids A* **5,** 1703 (1993).
19. J. R. Richards, A. M. Lenhoff, and A. N. Beris, *Phys. Fluids* **6,** 2640 (1994).
20. J. R. Richards, A. N. Beris, and A. M. Lenhoff, *Phys. Fluids* **7,** 2617 (1995).
21. M. Renardy and Y. Renardy, *Phys. Fluids A* **5,** 2738 (1993); *Phys. Fluids A* **6,** 3502 (1994).
22. A. V. Coward and Y. Renardy, Small amplitude oscillatory forcing on two-layer plane channel flow, *J. Fluid Mech.* **334,** 87 (1997).
23. C.-S. Yih, *J. Fluid Mech.* **26,** 337 (1967).
24. J. R. Richards, Ph.D. Thesis, Department of Chem. Eng., University of Delaware, 1994.
25. S. V. Patankar, *Numerical Heat Transfer and Fluid Flow* (Hemisphere, New York, 1980).
26. C. W. Hirt and B. D. Nichols, *J. Comput. Phys.* **39,** 201 (1981).
27. D. L. Youngs, Time-dependent multi-material flow with large fluid distortion, in *Numerical Methods for Fluid Dynamics,* edited by K. W. Morton and M. J. Baines (Academic Press, New York, 1982), pp. 273–285.
28. D. L. Youngs, An interface tracking method for a 3d Eulerian hydrodynamic code, Technical Report 44/92/35, AWRE, 1984 (unpublished).
29. W. J. Rider *et al.*, Accurate solution algorithms for incompressible multiphase fluid flows, Technical Report AIAA 95-0699, 1995 (unpublished).
30. W. F. Noh and P. Woodward, The *SLIC* (simple line interface calculation) method, Technical Report UCRL-52111, Lawrence Livermore Laboratory, 1976 (unpublished).
31. N. Ashgriz and J. Y. Poo, *J. Comput. Phys.* **93,** 449 (1991).
32. L. A. Jurman, S. E. Deutsch, and M. J. McCready, *J. Fluid Mech.* **238,** 187 (1992).
33. M. Sangalli *et al.*, *Chem. Eng. Sci.* **47,** 3289 (1992).